Analyses of the Evolution of Iron-Silicide Precipitates in Multicrystalline Silicon During Solar Cell Processing

Jonas Schön, Antti Haarahiltunen, Hele Savin, David P. Fenning, Tonio Buonassisi, Wilhelm Warta, and Martin C. Schubert

***Abstract*—We simulate the precipitation of iron during the multicrystalline ingot crystallization process and the redistribution of iron during subsequent phosphorus diffusion gettering with a 2-D model. We compare the simulated size distribution of the precipitates with the X-ray fluorescence microscopy measurements of iron precipitates along a grain boundary. We find that the simulated and measured densities of precipitates larger than the experimental detection limit are in good agreement after the crystallization process. Additionally, we demonstrate that the measured decrease of the line density and the increase of the mean size of the iron precipitates after phosphorus diffusion gettering can be reproduced with the simulations. The size and spatial distribution of iron precipitates affect the kinetics of iron redistribution during the solar cell process and, ultimately, the recombination activity of the precipitated iron. Variations of the cooling rate after solidification and short temperature peaks before phosphorus diffusion strongly influence the precipitate size distribution. The lowest overall density of iron precipitates after phosphorus diffusion is obtained in the simulations with a temperature peak before phosphorus diffusion, followed by moderate cooling rates.**

***Index Terms*—Gettering, impurities, semiconductor process modeling.**

I. Introduction

IRON can be found in almost all directionally solidified silicon ingots, where it is dissolved in the interstitial state and precipitated at grain boundaries and dislocations. The charge-carrier lifetime of the as-cut wafers is often limited by interstitial iron, although the interstitial iron concentrations are usually small compared with the total concentrations [1], [2]. It is well known that precipitated iron is less recombination active than interstitial iron [3]. Although the recombination activity of individual precipitates increases with their size, a low density of large precipitates should be favored over a high density of small ones with respect to the charge-carrier lifetime [4]. Besides their direct impact on the charge carrier lifetime, the size and spatial distribution of iron precipitates determine dissolution and precipitation during processing, thus affecting the interstitial iron concentration [5]. During phosphorus diffusion, interstitial iron is highly mobile and diffuses into the phosphorus-doped regions. The interstitial iron concentration in the bulk can be reduced by one or two orders of magnitude during phosphorus diffusion [6]–[9], although precipitated iron starts to dissolve. For this reason, precipitates become more important for the charge-carrier lifetime after phosphorus diffusion than in the as-grown state [7]. The widely discussed low-temperature anneal (LTA) [10], [11] further reduces the concentration of interstitial iron and increases the relevance of iron precipitates. The gettering of precipitated iron is limited by dissolution [12], and thus, high temperatures are necessary. In multicrystalline (mc)-Si with medium to high iron concentrations, a complete precipitate dissolution results in high interstitial iron concentration after standard phosphorus diffusion due to the limited gettering capacity. However, even without complete dissolution, a reduction of the iron precipitate density should be possible by applying an appropriate anneal at high temperature.

Precipitation and gettering models are primarily used for the simulation of interstitial iron concentration [13]–[16], which can be easily compared with measurements. Densities of iron precipitates in mc-Si after the crystallization process were previously simulated with a 0-D model [17], which takes nucleation and growth of iron-silicide precipitates into account. However, a direct experimental verification of the density and size of precipitates is rather difficult. The simulated sizes of precipitates in solar grade silicon range from few iron atoms to several 10^8, with a corresponding radius between 0.2 and 100 nm. Large iron-rich precipitates may be detected by synchrotron-based X-ray fluorescence microscopy (μ-XRF) [18]. The further development of this method over the past years improved the detection limit to roughly 3×10^4 atoms/precipitate [19], which allows direct comparison between the simulated and measured size distribution for large precipitates.

This study aims to employ simulation toward explaining the distribution of iron in mc-Si and should help to clarify the role of precipitates in limiting charge-carrier lifetime. We investigate the evolution of iron-silicide precipitates during the

Manuscript received ; revised ; accepted . This work was supported in part by the German Ministry for the Environment, Nature Conservation and Nuclear Safety under Contract 0325270G (SolarWinS), in part by the Fraunhofer Society in the frame of the Si-Beacon project, and in part by the U.S. National Science Foundation (NSF) and the U.S. Department of Energy under Grant NSF CA No. EEC-1041895. The work of D. P. Fenning was supported by an NSF Graduate Research Fellowship.

J. Schön, W. Warta and M. C. Schubert are with the Fraunhofer Institute for Solar Energy Systems, 79100 Freiburg, Germany (e-mail: jonas.schoen@ise.fraunhofer.de; wilhelm.warta@ise.fraunhofer.de; martin.schubert@ise.fraunhofer.de).

A. Haarahiltunen and H. Savin are with the Aalto University, FI-00076 Aalto, Finland (e-mail: antti.haarahiltunen@aalto.fi; hele.savin@aalto.fi).

D. P. Fenning and T. Buonassisi are with the Massachusetts Institute of Technology, Cambridge, MA 02139 USA (e-mail: dfenning@mit.edu; buonassisi@mit.edu).

Color versions of one or more of the figures in this paper are available online at http://ieeexplore.ieee.org.

Digital Object Identifier 10.1109/JPHOTOV.2012.2212699

crystallization process and further processing steps by simulation. We compare the simulated results for a grain boundary with μ-XRF measurements to verify our model quantitatively. On the basis of the successful verification, we analyze and discuss the possibilities to optimize the distribution of precipitated iron by varying the temperature sequences.

II. Model

We simulate the size distribution of iron-silicide precipitates using the Fokker–Planck equation for the precipitation as presented in [7]. In the precipitation model, an effective local solubility [13] and radius [20], depending on the size of precipitates, are used for the calculation of the dissolution and growth rates of iron-silicide precipitates, together with the iron diffusivity value from [3]. We assume that the density of nucleation sites is proportional to the density of crystal defects, i.e., grain boundaries and dislocations, with a nucleation site line density along dislocations of 3.3×10^5 cm^{-1} [7]. Precipitates grow only at a small fraction of the nucleation sites, and a moderate increase of the line density of the nucleation sites along dislocations affects the precipitate densities only slightly. For small iron-silicide precipitates, the flux of iron to the precipitates is determined by the effective radius of the nucleation sites [21], which is $r_{\mathrm{SD}} = 15$ nm in our simulations [7]. All the parameters that were used in the precipitation model were fitted to measurements of interstitial iron concentration in the previous works [7], [13], [20]. The model allows not only the nucleation of new precipitates, but also the partial dissolution of precipitates. Thus, a minimization of the precipitate density in the simulations is possible.

The emitter formation is simulated with the phosphorus diffusion model from [22]. The model for phosphorus diffusion gettering is based on the effect of segregation of dissolved iron into the emitter, due to an increased solubility in highly phosphorus-doped silicon. The model including the segregation coefficient is also taken from [7].

The process time, the temperature, the phosphorus concentration in the phosphorus source, the total iron concentration, and the geometry of the simulated grain are required as inputs for the simulations. In Fig. 1, the 2-D structure is shown, which is used for the crystallization and the phosphorus diffusion process. The model structure represents the upper left quarter of a grain with 3 mm width and includes a small grain boundary on the left side as well as detached dislocations within the grain. The mean dislocation density inside the grain is 1×10^4 cm^{-2}. The nucleation site density at a mesh point with one dislocation is calculated by dividing the line density along dislocations (3.3×10^5 cm^{-1}) by the size of the mesh point. The influence of the dislocation cluster included in [7] on the presented results in Sections III and IV is small, and thus, only half of the model structure of [7] was taken for the simulations to minimize the computing time. The model structure is 2-D to account for the simultaneous external gettering to the wafer surface (vertical) and the lateral diffusion of iron due to inhomogeneously distributed crystal defects. The thickness of the model structure is only half of the wafer thickness, taking advantage of the mirror symmetry during phosphorus diffusion from both sides.

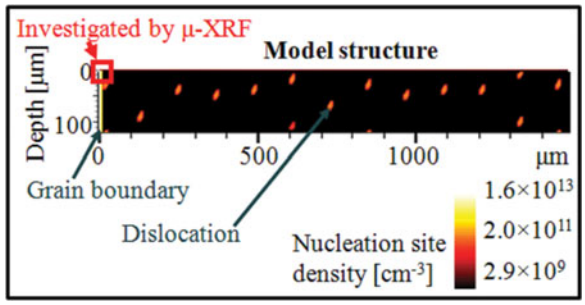

Fig. 1. Schematic view of our model structure, representing a quarter of a typical grain (3 mm in width). The grain boundary is visible on the left. The nucleation sites are placed at the grain boundary and along the dislocations (orange) within the grain. For the comparison with the experiments, we investigated the precipitate line densities along the grain boundary of our model structure to a depth of 8 μm, which is the approximated information depth of the μ-XRF setup from [19] (indicated by the red rectangle). Note that the small red line at the top of the structure is a phosphorus source that is turned on during the phosphorus diffusion step.

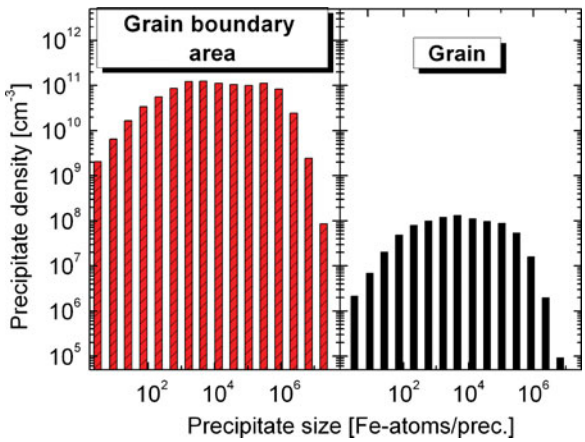

Fig. 2. Simulated iron-silicide precipitate size distribution after crystallization at a grain boundary (left) and inside a grain (right). For a better comparison, the densities in an area around the grain boundary are calculated from the areal density at the grain boundary. We assume a width of 0.2 μm for this grain boundary area.

At a certain temperature during the crystallization process, the homogeneously distributed interstitial iron diffuses from the grain to the nucleation sites, precipitates, and increases the total iron concentration at the grain boundary. However, the total amount of iron within the grain is higher than the amount of iron at the grain boundary after typical crystallization processes. For fast cooling processes, the iron remains dissolved, whereas it precipitates at the isolated dislocations within the grain for slow cooling processes. For a cooling rate of 3.5 K/min, representative of the latter case, the resulting precipitate size distributions can be seen in Fig. 2. The densities are almost three orders of magnitude higher in the area of the grain boundary, assuming a width of 0.2 μm for the grain boundary in the calculation of the precipitate density, which is the maximum expected precipitate diameter and the spot size of the X-ray beam in [19]. Thus, the higher densities in the grain boundary area compared with the grain illustrate the higher probability for detection. For

an experimental verification of the simulated results inside the grain, a measurement of a few dislocations will be not enough, taking the expected line density of 2.5 μm^{-1} for detectable precipitates along a dislocation into account. The exact number of dislocations, which have to be analyzed for sufficient statistics, depends on the measurement setup and the angle between surface and dislocation. The simulated precipitate size distribution inside the grain is shifted toward smaller precipitates with only a fourth of the mean size of the precipitates at the grain boundary (see Fig. 2). This shift toward smaller precipitates is supported by the measurements at dislocations inside the grain in [23].

III. Experimental Verification

In [19], iron-silicide precipitates along 35 μm of a random-angle grain boundary with a misorientation of 44.5° were measured with μ-XRF. The three analyzed samples were cut from sister wafers close to the edge of the mc-Si ingot. The detection limit in the μ-XRF setup from [19] was 3×10^4 iron atoms. The full-width half-maximum spot size of the X-ray beam was 200 nm, and the approximated information depth was 8 μm. In the comparison between simulation and measurement, we concentrate on the measured section of the grain boundary (see Fig. 1) and average the simulated precipitate densities at the grain boundary until the approximated information depth.

The simulation of the as-cut sample starts after solidification. Total iron concentrations of up to 1×10^{15} cm^{-3} were reported at the edge of an ingot [19], [24]. At a distance of 2 cm from the edge, the total iron concentration is typically decreased to 1×10^{14} cm^{-3}. We use this concentration as the initial iron concentration in the following simulations. An ingot cooling rate of 3.5 K/min is chosen for temperatures below 1100 °C. The temperature profiles for the 60 min LTA at 500 °C and the phosphorus diffusion process at 900 °C are taken from [19]. In the simulation, an initial phosphorus concentration in the phosphorus silicate glass is used that results in a sheet resistance of 40 Ω/□.

In Fig. 3, the simulated line densities of iron-silicide precipitates as a function of precipitate size (a) before and (c) after phosphorus diffusion, as well as the results for processes (b, d) with additional LTA, are shown. The simulated variation of the line densities of precipitates with less than 3×10^4 iron atoms between the different processes is rather large. The densities of these precipitates are of the same order or smaller than the densities of larger precipitates. Thus, the fraction of precipitated iron that is not detectable with the μ-XRF setup of [19] is small according to our simulations. In addition, the recombination activity of these precipitates is smaller than for large precipitates [25], and thus, their influence on the charge-carrier lifetime should be small compared with larger precipitates of similar density. In all four cases, the precipitate density decreases rapidly for very large precipitates with more than 5×10^6 iron atoms.

The simulated densities of precipitates with moderate sizes, like those which were measured in [19], differ significantly between the as-cut sample [see Fig. 3(a)] and the samples after phosphorus diffusion [see Fig. 3(c) and 3(d)]. The simulated densities of precipitates with iron atoms between

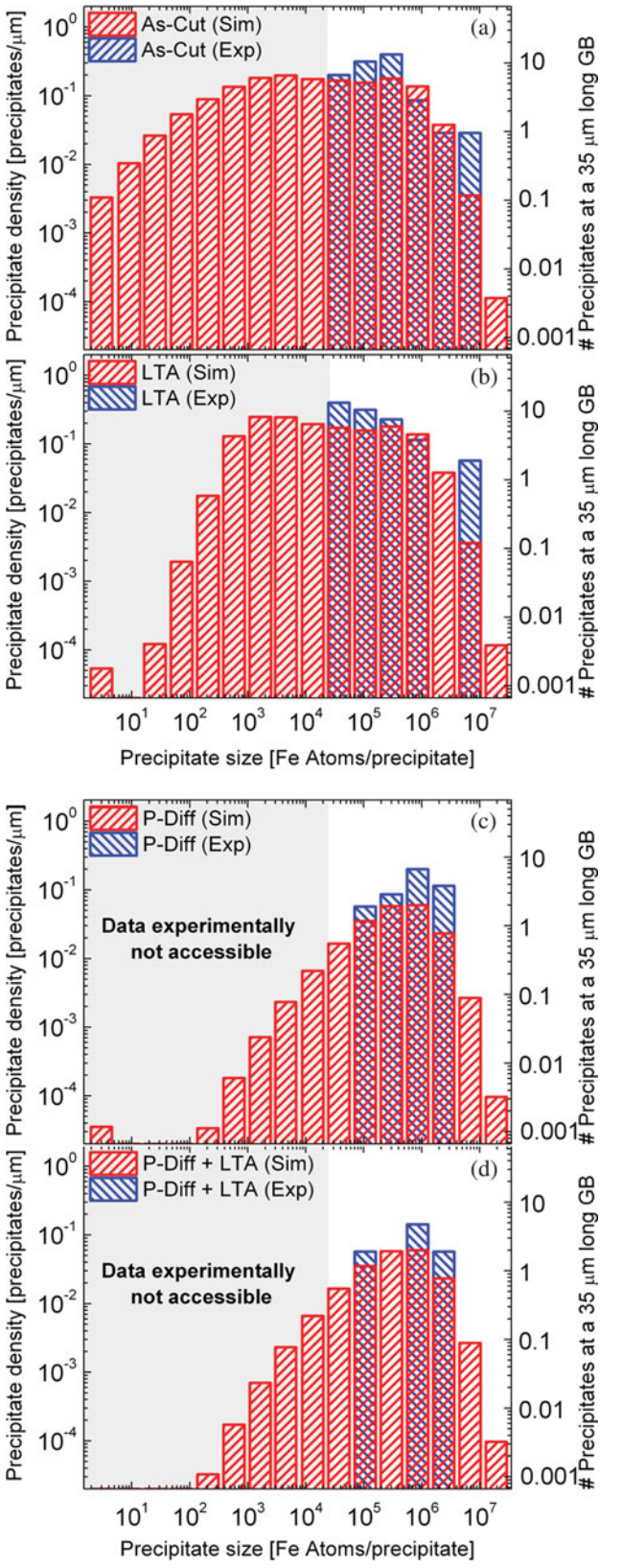

Fig. 3. Comparison of the measured (from [19]) and simulated line densities of different iron-silicide precipitate sizes before phosphorus diffusion (a) without LTA, (b) with LTA, (c) after phosphorus diffusion, and (d) after phosphorus diffusion with LTA. At the right y-axes the corresponding number of measured or expected precipitates along 35 μm of the investigated grain boundary [19] are shown.

TABLE I
MEAN NUMBERS OF IRON ATOMS PER IRON-SILICIDE PRECIPITATE AT A GRAIN BOUNDARY UP TO A DEPTH OF 8 μm AS WELL AS THE LINE DENSITY OF PRECIPITATE (PRECIPITATES/μm) ARE LISTED FOR SIMULATED AND MEASURED SAMPLES

Sample	Simulation	Experiment
	Mean size [atoms/prec.]	
As-Cut	4.6×10^5	5.3×10^5
As-Cut + LTA	4.5×10^5	5.0×10^5
P-Diffusion	7.6×10^5	10×10^5
P-Diffusion + LTA	7.6×10^5	9.0×10^5
	Line density [prec./μm]	
As-Cut	0.68	1.2
As-Cut + LTA	0.69	1.3
P-Diffusion	0.20	0.4
P-Diffusion + LTA	0.20	0.2

Only precipitates with more than 3×10^4 iron atoms are considered.

3×10^4 and 5×10^5 are reduced by 70–90% due to phosphorous diffusion. Similar decrease of the detected precipitates in this size range was also found in the experiments of [19]: five (without LTA) and two precipitates (with LTA) instead of 32 before phosphorus diffusion. For large precipitates, the fraction of iron that dissolves is small, and thus, the densities of larger precipitates stay almost constant.

In Table I, the mean sizes of precipitates above the detection limit are summarized, and the increase of the mean size during phosphorus diffusion, due to dissolution of small and medium precipitates, can be clearly seen. However, precipitates of all sizes dissolve to some extent, and the density of large precipitates does not increase, as in high-temperature steps without phosphorus diffusion [7], according to the simulations. Note that the number of measured precipitates in [19] is small (16 after phosphorus diffusion), and a measured line density of 0.03 μm^{-1} corresponds to only one precipitate. Therefore, besides the measurement uncertainties, the influence of natural variation in the measured precipitate distribution must be considered, which could be quite significant between sister wafers [26]. For this reason, it is not possible to distinguish whether the measured increase of the density of precipitates with 4×10^6–3×10^7 iron atoms during phosphorus gettering [see Fig. 3] is due to a small effect of Oswald ripening or statistical noise between sister wafers.

In addition to the mean size, the total measured and simulated line densities are shown in Table I. The uncertainties in the measurements, due to the dependence of the signal on the depth of the precipitate, are negligible in the sum of the measured line densities. The grain boundary in [19], was chosen to be a large internal iron sink. In contrast, the model parameters that influence the precipitation behavior were fitted to mean interstitial iron concentrations [7], [13], [20] and should be interpreted as averaged values. This could be the reason for the slightly higher line densities in the measurements. Another effect that is able to artificially increase the measured line densities of precipitates above the detection limit is colonies of small precipitates that are counted as one large precipitate.

During the LTA, subsequent to the crystallization process [see Fig. 3(b)], a growth of smaller precipitates was observed in the simulated densities, resulting in a slight increase of the line density of precipitates above the detection limit. In the corresponding measurement, the density of precipitates with medium size was also higher after LTA [see Fig. 3(b)] than before [see Fig. 3(a)]. The same sample was measured before and after LTA. Thus, smaller differences are more reliable than in the measurements after phosphorus diffusion.

After phosphorus diffusion, the simulated line densities exhibit even smaller differences between the process with [see Fig. 3(c)] or without LTA [see Fig. 3(d)]. The measurement after phosphorus diffusion with additional LTA is not able to verify this result, due to the superposition with the statistical fluctuation between sister wafers. However, the differences to the as-cut sample are significant and confirm the decrease during phosphorus diffusion: the line densities measured at parallel wafers were three times (without additional LTA) and six times (with additional LTA) smaller than in the as-cut state (see Table I). In both measurements and the simulations, the increase of the average size of precipitates is of the same magnitude.

It should be noted that a moderate increase of the total iron concentration mainly increases the mean size of the precipitates and affects only slightly the precipitate density.

IV. OPTIMIZATION OF THE SIZE DISTRIBUTION

As an application of the successfully validated modeling procedure, we present in the following results of a study how to optimize the iron precipitate size distribution. Obviously, the smallest impact of precipitates is gained with a complete dissolution of the unavoidable precipitates after the crystallization process in combination with avoidance of nucleation in the following phosphorus diffusion process. This is typically not recommended in mc-Si with moderate or high iron concentration, due to the remaining high iron concentration after standard phosphorus diffusion and the excessive length of a gettering process aiming at a complete external gettering of iron. As an alternative, the size distribution of precipitates could be manipulated by variations of the temperature sequences.

The iron distribution after the crystallization process is determined by the cooling sequence for temperatures where the solubility falls below the total iron concentration. Supersatured iron tends to form energetically favorable, large precipitates during a slow cooling process. With increasing ingot cooling rate, an increasing fraction of the supersaturated iron is no longer able to reach existing precipitates, and the spatial distribution becomes more homogeneous. As a consequence, the resultant highly supersatured iron atoms stay dissolved or form small precipitates, if they are able to reach a nucleation site. Thus, the density of the small precipitates and the interstitial iron concentration after the crystallization process increase rapidly for faster cooling rates (see the black lines in Figs. 4 and 5).

If only the results after the crystallization process are considered (see the black lines in Figs. 4 and 5), a slow ingot cooling process is preferable. However, the efficiency of the gettering of interstitial and precipitated iron during phosphorus diffusion

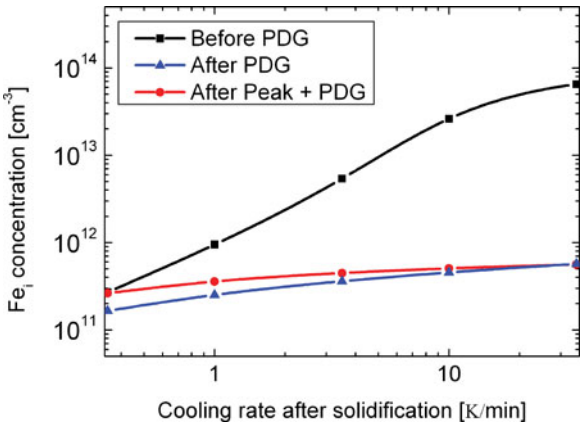

Fig. 4. Interstitial iron concentration after the crystallization process and additional phosphorus diffusion with and without a preceding temperature peak at 950 °C in dependence on the ingot cooling rate after solidification.

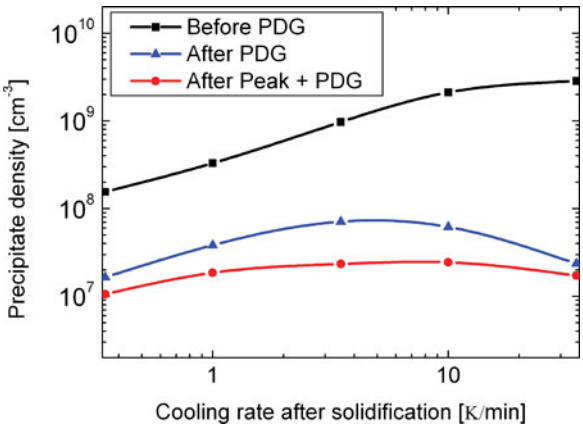

Fig. 5. Overall density of precipitates after the crystallization process and additional phosphorus diffusion with and without a preceding temperature peak at 950 °C in dependence on the cooling rate after solidification.

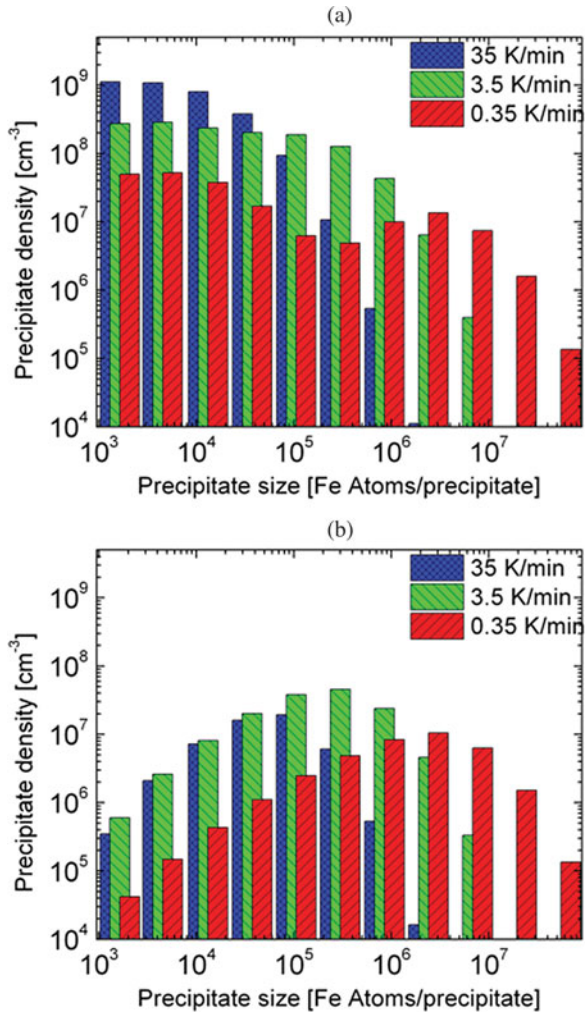

Fig. 6. Precipitate size distribution of the whole model structure (see Fig. 1) (a) before and (b) after phosphorus diffusion without preceding temperature peak for three different cooling rates during crystallization process.

depends on the iron distribution. We simulated a phosphorus diffusion process of 6 min duration at 900 °C, as in [19], subsequent to the different crystallization processes to quantify this effect. We chose a cooling rate of 40 K/min in the phosphorus diffusion process, which is slower than that in the previous section, to avoid the fact that in some cases, the precipitate density is dominated by very small precipitates (few atoms). These small precipitates could form during fast cooling with high interstitial concentration, i.e., after a fast crystallization process.

In Fig. 6, the size distributions before and after the standard phosphorus diffusion for three different cooling rates during the crystallization process are shown. The differences in Fig. 6 demonstrate the importance of the ingot cooling sequence for the final iron precipitates distribution in the solar cell. Although the temperature for the phosphorus diffusion is quite high and the size distribution shifts strongly during phosphorus diffusion, the three different crystallization processes stay distinctly different after the diffusion step. The density of larger precipitates, which typically include most of the precipitated iron, is reduced only slightly during phosphorus diffusion. For cooling rates of 35 K/min, the situation differs from processes with slower cooling rates, and most of the iron is already dissolved or gets dissolved during phosphorus diffusion at 900 °C. Gettering is more effective after fast ingot cooling rates, due to the high fraction of interstitial iron (see Fig. 4). The more effective gettering after fast cooling rates results in a lower concentration of precipitated iron, as well as a lower precipitate density, compared with moderate cooling rates (see Fig. 5). The highest precipitate density after phosphorus diffusion is simulated for a cooling rate of 3.5 K/min after solidification. After slow cooling during the crystallization process, the precipitates are larger, and iron does not redistribute as strongly as in the previously discussed case. The dissolution is slower, and phosphorus diffusion gettering is less effective. However, also after phosphorus diffusion, the simulated interstitial iron concentration decreases with decreasing cooling rate in the crystallization process, although the differences are much smaller than before phosphorus diffusion (see Fig. 4).

It was found in several experiments that gettering in areas with a high density of crystal defects is less effective [7], [27]. These areas typically limit the potential of mc solar cells. Therefore,

it should be noted that, besides the interstitial iron concentration [7], the precipitate density at the grain boundary is less reduced during phosphorus diffusion compared with the density inside the grain. This could be explained with the higher total iron concentration and precipitate density at the grain boundary, which impedes the dissolution of precipitates. The effect is most pronounced for slow cooling rates in the crystallization process, for which the reduction of the precipitate density inside the grain is three times higher than at the grain boundary.

In [7], an increase of the charge-carrier lifetime due to a temperature peak at 900 °C before phosphorus diffusion was observed. No phosphorus diffusion takes place during the temperature peak. The peak aims at dissolution of some of the precipitates to increase the efficiency of external gettering and to concentrate the residual iron in a few precipitates [7], [12]. The higher total iron concentration and the higher temperatures during phosphorus diffusion in the process applied in Section III suggest a peak temperature around 950 °C or higher. For high total iron concentrations, as they are measured, e.g., in areas that are influenced by the contamination from the crucible, care has to be taken that not all precipitates dissolve during the peak. Otherwise, the standard phosphorus diffusion gettering is not strong enough to reduce the dissolved iron to an acceptable concentration. In some of these cases, a combination of complete dissolution and extended gettering at low temperature, at which precipitates nucleate again, is an alternative.

We simulated phosphorus diffusion with a preceding temperature peak at 950 °C for 5 min, followed by a fast cooling to 900 °C (80 K/min). The simulated overall precipitate densities after phosphorus diffusion with temperature peak are shown in Fig. 4 for the various cooling rates during crystallization. In the presented simulations, the differences between the interstitial iron concentration with or without temperature peak were found to be small (see Fig. 4).

The temperature peak at 950 °C has the strongest impact on the precipitate density for a cooling rate of 3.5 K/min during the crystallization process. Precipitates are dissolved during the higher temperatures and afterward effectively gettered. In comparison with medium cooling rates, the line density is less affected by the temperature peak before phosphorus diffusion for slow cooling rates in the crystallization process. In this case, the duration of the peak is too short to dissolve the existing large precipitates completely. After a very fast cooling sequence in the crystallization process, most of the iron is in small, easily dissolvable precipitates or in the interstitial state, and a temperature peak has almost no influence.

In the simulated phosphorus diffusion, a large fraction of small and moderate precipitates are already dissolved in the standard phosphorus diffusion at 900 °C. Therefore, we expect an even higher impact of the temperature peak on the line density of precipitates for phosphorus diffusion processes with lower temperatures.

V. Conclusion

The size distributions of iron precipitates at a grain boundary after crystallization and further processing steps were simulated with a model based on the Fokker–Planck equation, which has been previously demonstrated to successfully describe the interstitial iron concentration [7]. The agreement between μ-XRF measurements and the simulations of the precipitate size-distribution at a grain boundary before and after phosphorus diffusion is within the statistic fluctuation. Additionally, the measured and simulated evolutions of the mean size and the line density of the iron precipitates during processing steps are in good agreement.

Furthermore, we investigated the possibilities to influence the size distribution by different process sequences. There are two options in the crystallization process. 1) A slow cooling rate below temperature of 1000 °C should be preferred as long as the gettering capacity of the phosphorus diffusion step is small compared with the total iron concentration. 2) A fast cooling rate after crystallization increases the interstitial iron concentration and the fraction of precipitates that dissolves during subsequent phosphorus diffusion according to the simulation. This effect increases the gettering efficiency of the phosphorus diffusion. With a cooling rate of 35 K/min during the crystallization process, the line density after phosphorus diffusion is almost as small as with slow cooling, but the precipitates are smaller, which should lead to less recombination of charge carriers at precipitates.

For the transfer of the obtained results into charge-carrier lifetimes [25], [28], the interstitial iron concentrations have to be considered. However, the differences in the interstitial iron concentrations between the simulated processes are rather small. A slower cooling rate or a LTA at the end of the phosphorus diffusion process, aiming for a reduced interstitial iron concentration, could be incorporated into the phosphorus diffusion process independent of the presented modifications.

A temperature peak before phosphorus diffusion could be used to manipulate the size distribution of precipitates. The gettering efficiency of the phosphorus diffusion is increased by a preceding temperature peak comparable with fast cooling in the crystallization process. The temperature peak at 950 °C for 5 min before phosphorus diffusion reduces the precipitate density most effectively after a moderate cooling process at around 3.5 K/min after solidification. In contrast to the high-temperature preanneal, a LTA affects the line density and the size distribution only slightly as confirmed previously experimentally [19]. We concentrated on an iron concentration of 1×10^{14} cm^{-3} but expect that a moderate variation of the initial iron concentration does not affect the qualitative results [29].

References

[1] D. Macdonald, A. Cuevas, A. Kinomura, Y. Nakano, and L. J. Geerligs, "Transition-metal profiles in a multicrystalline silicon ingot," *J. Appl. Phys.*, vol. 97, pp. 33523-(1–7), 2005.

[2] B. Sopori, "Silicon solar-cell processing for minimizing the influence of impurities and defects," *J. Electron. Mater.*, vol. 31, pp. 972–980, 2002.

[3] A. A. Istratov, H. Hieslmair, and E. R. Weber, "Iron and its complexes in silicon," *Appl. Phys. A*, vol. 69, pp. 13–44, 1999.

[4] T. Buonassisi, A. A. Istratov, M. A. Marcus, B. Lai, Z. Cai, S. M. Heald, and E. R. Weber, "Engineering metal-impurity nanodefects for low-cost solar cells," *Nat. Mater. Lett.*, vol. 4, pp. 676–679, 2005.

[5] T. Y. Tan, "Recent progresses in understanding gettering in silicon," in *Proc. MRS Spring Meeting*, 2000.

[6] R. Kvande, L. J. Geerligs, G. Coletti, L. Arnberg, M. Di Sabatino, E. J. Øvrelid, and C. C. Swanson, "Distribution of iron in multicrystalline silicon ingots," *J. Appl. Phys.*, vol. 104, pp. 064905-(1–9), 2008.

[7] J. Schön, H. Habenicht, M. C. Schubert, and W. Warta, "Understanding the distribution of iron in multicrystalline silicon after emitter formation: Theoretical model and experiments," *J. Appl. Phys.*, vol. 109, pp. 063717-(1–8), 2011.

[8] M. B. Shabani, T. Yamashita, and E. Morita, "Study of gettering mechanisms in silicon: Competitive gettering between phosphorus diffusion gettering and other gettering sites," *Solid State Phenomena*, vol. 131–133, pp. 399–404, 2008.

[9] V. Vähänissi, A. Haarahiltunen, H. Talvitie, M. Yli-Koski, and H. Savin, "Impact of phosphorus gettering parameters and initial iron level on silicon solar cell properties," *Prog. Photovolt: Res. Appl.*, (May 2, 2012). [Online]. DOI: 10.1002/pip.2215.

[10] M. Pickett and T. Buonassisi, "Iron point defect reduction in multicrystalline silicon solar cells," *Appl. Phys. Lett.*, vol. 92, pp. 122103-(1–3), 2008.

[11] M. Rinio, A. Yodyunyong, S. Keipert-Colberg, Y. P. B. Mouafi, D. Borchert, and A. Montesdeoca-Santana, "Improvement of multicrystalline silicon solar cells by a low temperature anneal after emitter diffusion," *Prog. Photovolt.*, vol. 19, pp. 165–169, 2011.

[12] P. S. Plekhanov, R. Gafiteanu, U. M. Gösele, and T. Y. Tan, "Modeling of gettering of precipitated impurities from Si for carrier lifetime improvement in solar cell applications," *J. Appl. Phys.*, vol. 86, pp. 2453–2458, 1999.

[13] A. Haarahiltunen, H. Väinölä, O. Anttila, M. Yli-Koski, and J. Sinkkonen, "Experimental and theoretical study of heterogeneous iron precipitation in silicon," *J. Appl. Phys.*, vol. 101, pp. 043507-(1–6), 2007.

[14] J. Hofstetter, D. P. Fenning, M. I. Bertoni, J.-F. Lelièvre, C. del Cañizo, and T. Buonassisi, "Impurity-to-efficiency simulator: predictive simulation of silicon solar cell performance based on iron content and distribution," *Prog. Photovolt.*, vol. 19, pp. 487–497, 2011.

[15] S. A. McHugo, H. Hieslmair, and E. R. Weber, "Gettering of metallic impurities in photovoltaic silicon," *Appl. Phys. A (Mater. Sci. Process.)*, vol. A64, pp. 127–137, 1997.

[16] A. Haarahiltunen, H. Savin, M. Yli-Koski, H. Talvitie, and J. Sinkkonen, "Modeling phosphorus diffusion gettering of iron in single crystal silicon," *J. Appl. Phys.*, vol. 105, pp. 023510-(1–4), 2009.

[17] A. Haarahiltunen, H. Savin, M. Yli-Koski, H. Talvitie, M. I. Asghar, and J. Sinkkonen, "As-grown iron precipitates and gettering in multicrystalline silicon," *Mater. Sci. Eng. B*, vol. 159–160, pp. 248–252, 2009.

[18] S. A. McHugo, H. Hieslmair, E. R. Weber, M. D. Rosenblum, and J. P. Kalejs, "Interactions of structural defects with metallic impurities in multicrystalline silicon," in *Proc. MRS Fall Meeting*, 1996.

[19] D. P. Fenning, J. Hofstetter, M. I. Bertoni, S. Hudelson, M. Rinio, J. F. Lelièvre, B. Lai, C. del Cañizo, and T. Buonassisi, "Iron distribution in silicon after solar cell processing: Synchrotron analysis and predictive modeling," *Appl. Phys. Lett.*, vol. 98, pp. 162103-(1–3), 2011.

[20] A. Haarahiltunen, H. Talvitie, H. Savin, O. Anttila, M. Yli-Koski, M. I. Asghar, and J. Sinkkonen, "Gettering of iron in silicon by boron implantation," *J. Mater. Sci.: Mater. Electron.*, vol. 19, pp. S41–S45, 2008.

[21] A. Haarahiltunen, H. Väinölä, O. Anttila, E. Saarnilehto, M. Yli-Koski, J. Storgårds, and J. Sinkkonen, "Modeling of heterogeneous precipitation of iron in silicon," *Appl. Phys. Lett.*, vol. 87, pp. 151908-(1–3), 2005.

[22] J. Schön and W. Warta, "Simulation of phosphorus diffusion and iron gettering with sentaurus process," in *Proc. 23rd Eur. Photovoltaic Sol. Energy Conf.*, Valencia, Spain, 2008, pp. 1851–1854.

[23] M. I. Bertoni, D. P. Fenning, M. Rinio, V. Rose, M. Holt, J. Maser, and T. Buonassisi, "Nanoprobe X-ray fluorescence characterization of defects in large-area solar cells," *Energy Environ. Sci.*, vol. 4, pp. 4252–4257, 2011.

[24] S. Riepe, I. E. Reis, W. Kwapil, M. A. Falkenberg, J. Schön, H. Behnken, J. Bauer, D. Kreßner-Kiel, W. Seifert, and W. Koch, "Research on efficiency limiting defects and defect engineering in silicon solar cells—Results of the German research cluster SolarFocus," *Phys. Status Solidi (C)*, vol. 8, pp. 733–738, 2010.

[25] P. S. Plekhanov and T. Y. Tan, "Schottky effect model of electrical activity of metallic precipitates in silicon," *Appl. Phys. Lett.*, vol. 76, p. 3777, 2000.

[26] A. Zuschlag, S. Ohl, J. Bernhard, H. Morhenn, J. Ebser, J. Junge, S. Seren, and G. Hahn, "μXRF investigations on the influence of solar cell processing steps on iron and copper precipitates in multicrystalline silicon," in *Proc. 35th IEEE Photovolt. Spec. Conf.*, Honolulu, HI, 2010, pp. 000347–000351.

[27] A. Bentzen, A. Holt, R. Kopecek, G. Stokkan, J. S. Christensen, and B. G. Svensson, "Gettering of transition metal impurities during phosphorus emitter diffusion in multicrystalline silicon solar cell processing," *J. Appl. Phys.*, vol. 99, pp. 093509-(1–6), 2006.

[28] M. C. Schubert, J. Schön, B. Michl, A. Abdollahinia, and W. Warta, "Modeling distribution and impact of efficiency limiting metallic impurities in silicon solar cells," in *Proc. 38th IEEE Photovolt. Spec. Conf.*, Austin, TX, 2012.

[29] J. Schön, A. Haarahiltunen, D. P. Fenning, T. Buonassisi, H. Savin, W. Warta, and M. C. Schubert, "Modeling the size distribution of iron silicide precipitates in multicrystalline silicon," in *Proc. 38th IEEE Photovolt. Spec. Conf.*, Austin, TX, 2012.

Authors' photographs and biographies not available at the time of publication.